frontiers | Frontiers in Physics

TYPE Original Research
PUBLISHED 10 January 2025
DOI 10.3389/fphy.2024.1503092

OPEN ACCESS

EDITED BY
Yi Wang,
Harbin Institute of Technology,
Shenzhen, China

REVIEWED BY
Yufei Hao,
Chinese Academy of Sciences (CAS), China
Shichen Bai,
Shandong University, China

*CORRESPONDENCE
Xi Lu,
xlu11@alaska.edu,
xi.lu@utdallas.edu
Terry Liu,
terryliuzixu@ucla.edu

RECEIVED 28 September 2024
ACCEPTED 10 December 2024
PUBLISHED 10 January 2025

CITATION
Lu X, Liu T, Chen X, Otto A and Zhang H (2025) Simultaneous observations of MHD hot flow anomaly and kinetic foreshock bubble and their impacts.
Front. Phys. 12:1503092.
doi: 10.3389/fphy.2024.1503092

Simultaneous observations of MHD hot flow anomaly and kinetic foreshock bubble and their impacts

Xi Lu[1,2]*, Terry Liu[3]*, Xingran Chen[1], Antonius Otto[1] and Hui Zhang[1]

[1]Geophysical Institute, University of Alaska Fairbanks, Fairbanks, AK, United States, [2]William B. Hanson Center for Space Sciences, University of Texas at Dallas, Richardson, TX, United States, [3]Department of Earth, Planetary, and Space Sciences, University of California, Los Angeles, Los Angeles, CA, United States

Hot flow anomalies (HFAs) and foreshock bubbles (FBs) are two types of transient phenomena characterized by flow deflected and hot cores bounded by one or two compressional boundaries in the foreshock. Using conjunction observations by the Time History of Events and Macroscale Interactions during Substorms (THEMIS) mission, we present an MHD HFA with a core filled with magnetosheath material around the bow shock and a typical kinetic FB associated with foreshock ions upstream of the bow shock, occurring simultaneously under the same solar wind/interplanetary magnetic field (IMF) conditions. The displacements of the bow shock moving back and forth along the sun-earth line are observed. Electron energy shows enhancements from ~50 keV in the FB to ~100 keV in the HFA core, suggesting additional acceleration process across the bow shock within the transient structure. The magnetosheath response of an HFA core-like structure with particle heating and electron acceleration is observed by the Magnetospheric Multiscale (MMS) mission. Ultralow frequency waves in the magnetosphere modulating cold ion energy are identified by THEMIS, driven by these transient structures. Our study improves our understanding of foreshock transients and suggests that single spacecraft observations are insufficient to reveal the whole picture of foreshock transients, leading to an underestimation of their impacts (e.g., particle acceleration energy and spatial scale of disturbances).

KEYWORDS

hot flow anomalies, foreshock bubbles, magnetohydrodynamics, bow shock, THEMIS

1 Introduction

Hot flow anomalies (HFAs) [1, 2] and foreshock bubbles (FBs) [3–8] are different types of transient structures in the Earth's foreshock region [9]. HFAs are characterized by one or two compressional boundaries and a low-density, heated core with significant

flow deflection [2]. The typical duration and spatial scale of HFAs are a few minutes and 1–2 R_E, respectively [10, 11], and they can extend away from the Earth's bow shock to 4.7 R_E [12]. FBs are observed as a density depletion accompanied by strong heating and flow deflection, followed by a shock boundary on the upstream side [5]. They typically measure 5–10 R_E along the solar wind flow direction [4, 13], and their transverse spatial scale can be as large as the foreshock width seen in global hybrid simulations [5].

A rotational discontinuity (RD) or a tangential discontinuity (TD) can transfer the kinetic energy of foreshock ions to thermal energy, leading to the development of HFAs or FBs through the Hall current driven by demagnetized foreshock ions upstream of the bow shock [14, 15]. In this study, we refer to these as kinetic HFAs and FBs, as they are generated from kinetic effects of foreshock ions. Although the FBs are first believed to be generated only by RDs in the solar wind [5], subsequent observations have shown that the TD can be an efficient driver for FBs as for HFAs [16] if the gyroradii of foreshock ions are larger than the thickness of TDs [3, 4, 17]. When the supersonic solar wind encounters the bow shock, some plasmas is reflected and transitions sunward (see review by [18]). An RD or TD can distort the magnetic field lines, which demagnetize the back-streaming foreshock ions. Depending on how the foreshock ions interact with the RD or TD, either an HFA with one or two compressional boundaries or an FB with a secondary shock can form due to different Hall current geometries through similar kinetic process (e.g., [19, 20]). The newly formed shock upstream of the FB can reflect incoming solar wind and generate a new foreshock region [21], while also accelerating particles through Fermi acceleration as it moves toward the bow shock [22, 23]. With the magnetic field piling up at the upstream shock, electrons can be energized to hundreds of keV through betatron acceleration [24]. Additionally, both observations and simulations show that HFAs and FBs can disturb the local bow shock and further affect the magnetosheath, magnetopause, and, consequently, the magnetosphere (e.g., [13, 25–27]).

MHD HFAs, on the other hand, can be described by MHD models and thus differ from kinetic HFAs (as well as FBs) in their processes of generation, locations, populations and core conditions [28–30]. MHD HFAs are produced by low-density flux tubes upstream of the bow shock, while kinetic HFAs are associated with discontinuities propagating along the bow shock surface [10, 14]. MHD HFAs are generated at the bow shock, whereas kinetic HFAs are generated upstream of the bow shock [2]. The ion distribution within MHD HFAs is more Maxwellian compared to that in kinetic HFAs, which are associated with suprathermal foreshock ions. The densities with the cores of kinetic HFA are consistently lower than the ambient solar wind density, while MHD HFAs exhibit density depletions in their cores relative to the ambient magnetosheath density. This is because MHD HFAs with high-density cores are generated through the interaction between low-density flux tubes and the oblique fast shock, which stretches denser magnetosheath plasmas outwards to fill the core region [28]. The earthward low-density flux tubes are not only solar wind structures but also include other foreshock transients with low density, such as foreshock cavities [31] and foreshock density holes (DHs) [32, 33], which convect with discontinuities that do not directly generate HFAs.

Previous studies show that either the kinetic process or the MHD method can independently form foreshock transients. In this study, conjugate observations reveal that these two formation mechanisms can coexist within a local area. Two spacecraft from the Time History of Events and Macroscale Interactions During Substorms (THEMIS) observed a kinetic FB and an MHD HFA simultaneously. This may enhance our understanding of HFAs and improve comprehension of foreshock transients. Understanding the formation mechanisms is a necessary step toward forecasting the disturbances driven by these transient structures.

2 Data

The Advanced Composition Explorer (ACE) and the Deep Space Climate Observatory (DSCOVR) are used to identify upstream solar wind discontinuities. At the Lagrange 1 (L1) point, solar wind plasma parameters (density, bulk velocity and temperature) are measured by the solar wind electron, proton and alpha monitor (SWEPAM) [34] aboard ACE [35, 36] and the Faraday cup boarded on DSCOVR [37, 38]. The available resolutions of the data from these two instruments are 64 s and ~4.5 s, respectively. Magnetic field data with a 1 s time resolution are provided by the magnetic field experiment (MAG) [39] on ACE and the magnetometer on DSCOVR.

Near the Earth's bow shock, THEMIS [40], consisting of three spacecraft (THA, THD and THE), provides plasma data measured by the electrostatic analyzer (ESA) [41] and magnetic field data from the fluxgate magnetometer (FGM) [42], both with a time resolution of ~2.76 s. The solid state telescope (SST) [43] provides pitch angle and energy spectra of suprathermal electrons.

The Magnetospheric Multiscale Mission (MMS) [44] is used to track the magnetosheath responses caused by foreshock transients. Fast survey mode data for plasma parameters (time resolution ~4.5 s) and magnetic fields (time resolution 1/16 s) are obtained from the fast plasma investigator (FPI) [45] and the flux magnetometers [46], respectively. The energetic particle detector (EDP) provides the electron spectrum (time resolution ~2.5 s) and the pitch angle distribution (time resolution ~19.7 s) through the fly's eye energetic particle sensor (FEEPS) [47].

3 Case study

Multi-point observations of THA and THE on 29 September 2017, show that an HFA with a high-density core (relative to the solar wind density) and a typical FB (Figure 1, marked by purple shadows) formed under the same IMF conditions at ~08:32 UT. Two spacecraft are situated close to the bow shock, with THE positioned nearer to the subsolar point (Figure 1O). They cross the bow shock from the magnetosheath into the foreshock at ~08:26 UT and return to the magnetosheath at ~08:37/08:38 UT (Figures 2E, 3E). The estimated geometries of the bow shock and magnetopause are from the bow shock model [48] and the magnetopause model [49], respectively (black curves in Figure 1O). The y-component of the magnetic fields (B_y) is ~0 on the downstream side of the transients and positive on the upstream side for both observations, indicating a discontinuity corresponding to the transient structures (Figures 1B, I). Before THA and THE return to the magnetosheath,

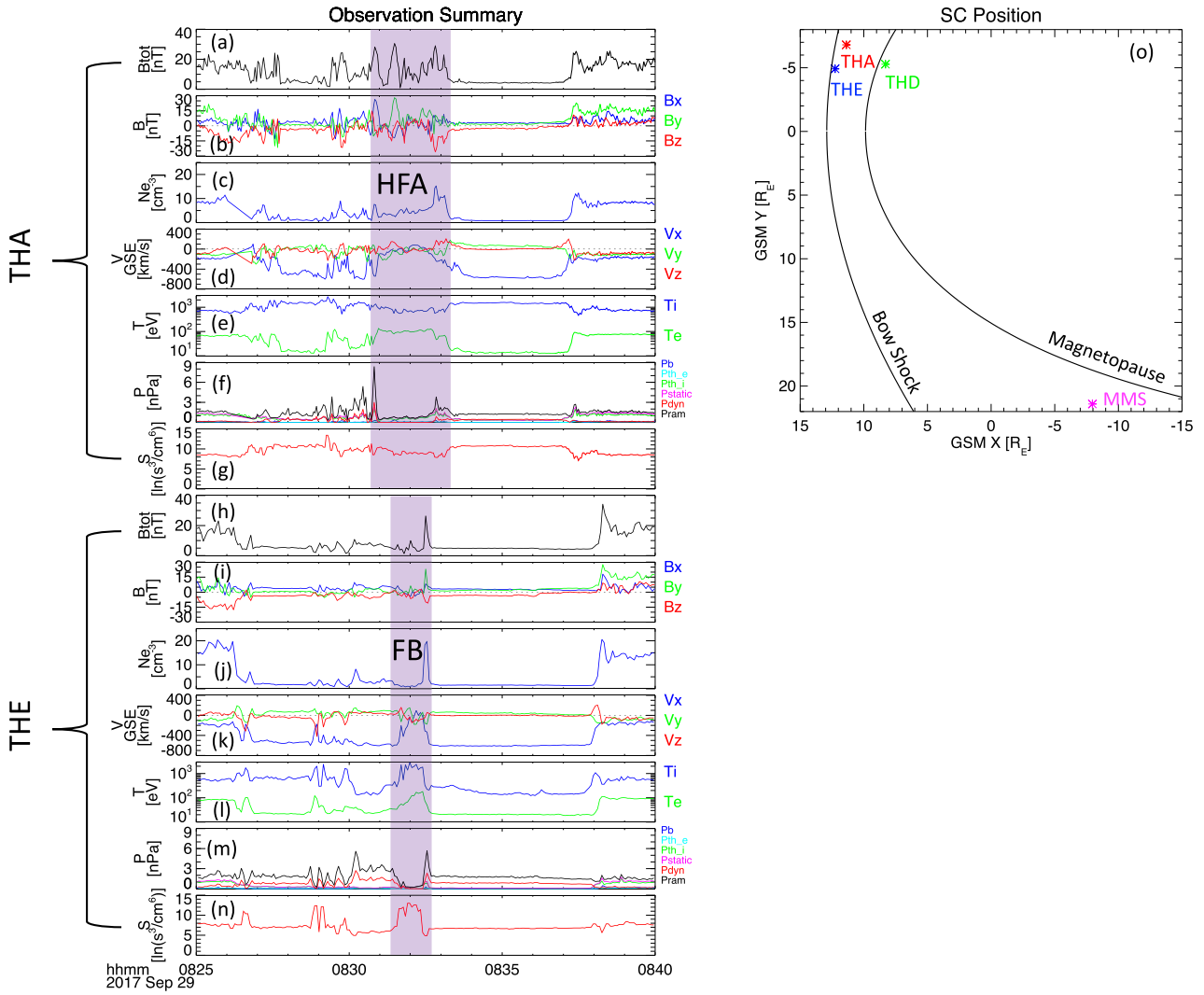

FIGURE 1
THA and THE observations of events on 29 September 2017, and the locations of the spacecraft in GSM coordinates. Panels **(A–G)** and **(I–N)** are magnetic field strength, magnetic field vectors in GSE coordinates, electron density, ion bulk velocity in GSE coordinates, electron and ion temperatures, pressures and the entropy for THA and THE, respectively. Panel **(O)** shows the positions of THA, THD, THE and MMS1 and the two black solid curves are the estimated bow shock and the magnetopause.

B_z changes from negative to 0 around 08:36 UT (Figures 1B, I), suggesting another discontinuity. The bow shock normal, derived from the shock crossings, is between [0.98, 0.02, −0.18] and [0.85, 0.14, −0.50] based on the coplanarity method ($\hat{\boldsymbol{n}}_s = \pm \frac{(\Delta \boldsymbol{B} \times \Delta \boldsymbol{V}) \times \Delta \boldsymbol{B}}{|(\Delta \boldsymbol{B} \times \Delta \boldsymbol{V}) \times \Delta \boldsymbol{B}|}$, where Δ represents the difference between the upstream value and downstream values of the quantities). Both spacecraft are in a quasi-parallel foreshock geometry ($\theta_{Bn} \approx 33° < 45°$) when they cross the bow shock into the solar wind (around 08:28 UT, Figures 1B, I).

The HFA observed by THA, located at [11.3, −6.2, −3.0] R_E in GSE coordinates, has two compressional boundaries in density (Figure 1C). Inside the core region, the electron density is greater than that of the ambient solar wind (~1 cm^{-3}) but lower than the magnetosheath value (~8 cm^{-3}). The flow is significantly deflected from earthward to sunward at the core (Figure 1D), and the temperatures of ions (~750 eV) and electrons (~100 eV) are comparable to those in the magnetosheath (Figure 1E). The total ram pressure ($P_{ram} = 2P_{dyn} + P_{th} + P_B$, where the dynamic pressure $P_{dyn} = n_e m_p v_n^2$, the thermal pressure $P_{th} = n_i k T_i + n_e k T_e$, and the magnetic pressure $P_B = \frac{B^2}{2\mu_0}$) reaches the maximum at the leading boundary (~08:30:50 UT) and drops to less than 1 nPa at the core (Figure 1F). The entropy of the single fluid ($S = -\frac{1}{n}\int d^3v\, f\, ln\, f$ in unit of ln(s^3/cm^6), where n is the number density in cm^{-3} and f is the phase space density distribution in s^3/cm^6) [50] is expressed as the integral of the particle distribution, and the result is overestimated by the foreshock ions in the ambient of the HFA (Figures 1G, 2E). These characteristics indicate that this HFA is an MHD HFA [28–30]. The energy of electrons increases from several keV to above 50 keV (Figures 2C, D), likely due to the betatron acceleration from the compressed magnetic field strength (Figure 2A) at the trailing boundary, moving into the core along the field lines [24]. The ion distributions in the core region are shown in the GSE-XY plane

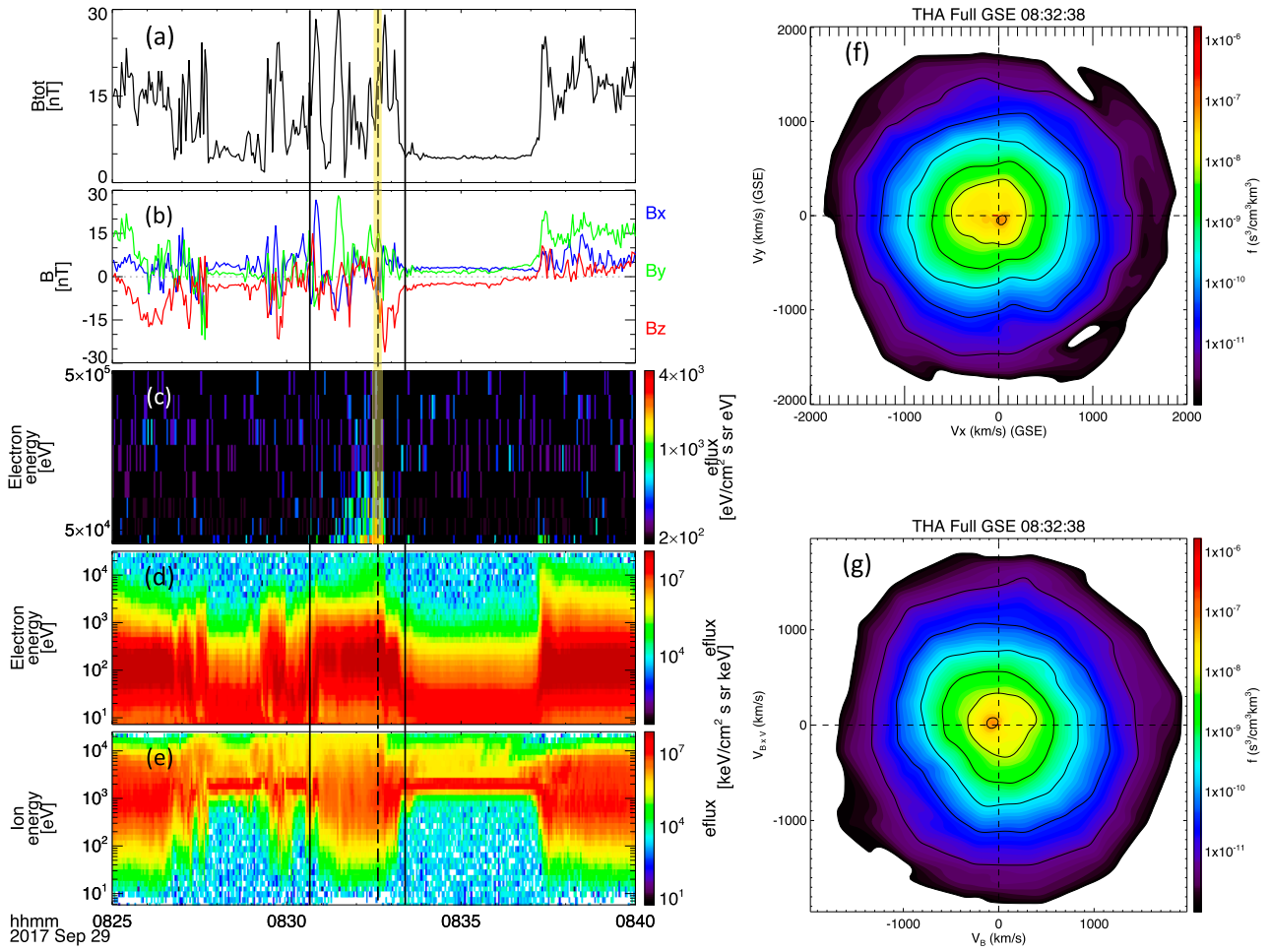

FIGURE 2
THA's observation of **(A)** magnetic field strength, **(B)** magnetic field vectors, **(C, D)** electron spectra, and **(E)** ion spectrum. The black solid lines mark the boundaries of the hot flow anomaly, and the dashed line marks the time of the velocity distributions in panel **(F)** and **(G)**. The energy enhancement is marked by yellow shadow in panels **(A–C)**.

(Figure 2F) and in the BE plane (where the *x*-axis is along the magnetic field direction and the *y*-axis contains the B × V vector) (Figure 2G). The core material consists of a single component (Figure 2E) and exhibits the asymmetry along the magnetic field lines (Figure 2G) [51].

The FB observed by THE, located at [12.2, −4.9 -1.6] R_E in GSE coordinates, shows a low-density core with compressions in magnetic field strength and electron density on the upstream side at ~08:32:30 UT (Figures 1H, J). Using the coplanarity method and mass flux conservation ($V_s = \frac{(n_u V_u - n_d V_d)\cdot \hat{\boldsymbol{n}}_s}{n_u - n_d}$, where the subscript *d* represents the downstream and *u* represents the upstream), we find that the upstream edge is propagating toward Earth with a speed of V_s = 238.12km/s and a normal $\hat{\boldsymbol{n}}_s$ = [−0.96, 0.26, 0.10], consistent with typical FBs (e.g., [7]). There is a strong deflection of the ion bulk flow, along with heating of both electrons and ions, and an enhancement of entropy in the core (Figures 1K, L, N). The total ram pressure drops to nearly 0 in the core and is significantly enhanced at the boundary (Figure 1M), which differs from the MHD HFA. Figures 3C, D show that electrons within the FB are energized to above 50 keV. The gradual increase in electron energy shown in Figure 3D is consistent with Fermi acceleration (see model comparison in Supplementary Figure S1 in the supplementary material) as the FB shock progressively propagates toward the bow shock [22]. Betatron acceleration [24] plays a minor role in the core region but likely dominates at the compressional boundary. For electrons above 30 keV, the acceleration appears weaker compared to that within the HFA. It is possible that the electrons accelerated by the FB could be further accelerated when reaching the HFA, potentially due to further field strength enhancement. The pitch angles of these electrons suggest a direction toward the upstream (Figure 3B), indicating that they are not from the solar wind but are associated with the bow shock and the transient structure. It is clear to see solar wind beam and foreshock ions in the ambient solar wind in the ion distributions (Figures 3F, K). Inside the FB, the solar wind beam weakens and becomes separated from foreshock ions (Figures 3G–J), which is distinct from the observations within the MHD HFA.

At the L1 point, ACE (located at [231.2, 40.8, −17.5] R_E in GSE coordinates) and DSCOVR (located at [227.7, −37.0, 10.4] R_E in GSE coordinates) identified two discontinuities in

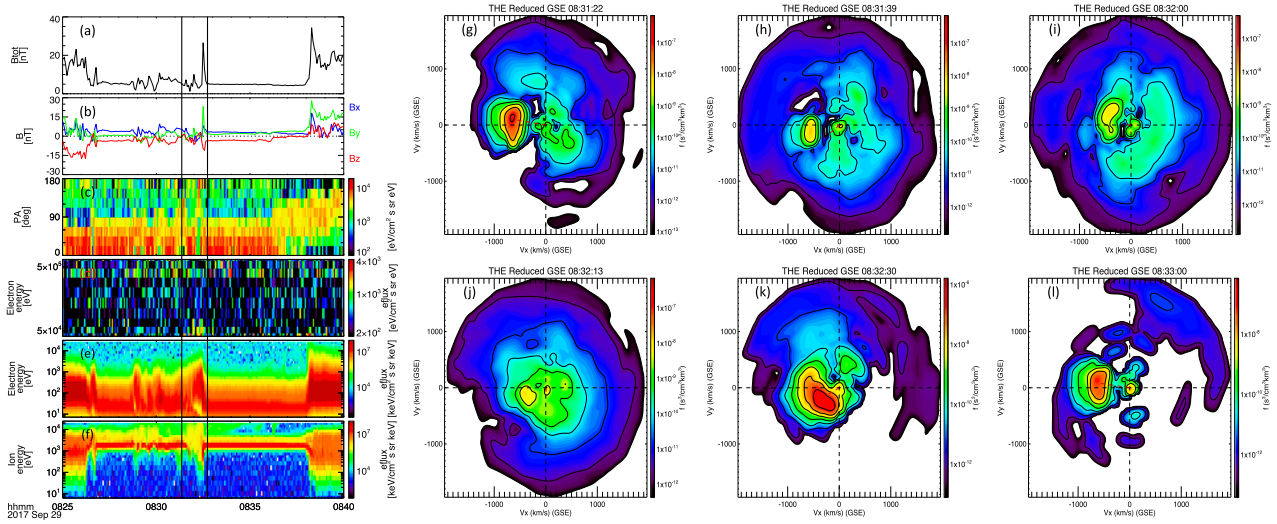

FIGURE 3
THE's observation of **(A)** magnetic field strength, **(B)** magnetic field vectors, **(C)** electron pitch angle for energy above 30 keV, **(D, E)** electron spectra and **(F)** ion spectrum. The black solid lines mark the boundaries of the foreshock bubble. Panels **(G–L)** are velocity distributions, where **(K)** is at the boundary, **(H–J)** are inside foreshock bubble's core and **(G)** and **(L)** are in the ambient solar wind.

the solar wind, indicated by changes in B_y from negative or ~0 to positive, and in B_z from negative to positive or ~0 (Figures 4B, C, H, I, marked by dashed lines; also see comparison in cone angle and clock angle in Supplementary Figure S2 in the supplementary material). The separation between the two discontinuities is 2–4 min, consistent with THEMIS observations. ACE does not show a clear density depletion (Figure 4D). Possibly due to its higher time resolution, DSCOVR observed multiple density depletion structures (Figure 4J), accompanied by proton temperature depletion as well (Figure 4K). Thus, these structures are not pressure balanced (Figure 4L), and their nature and origins remain unclear.

To further confirm that the first discontinuity, who contributes to the formation of the transients, is the same one observed by THEMIS, we compute the normal directions of it for comparison between THEMIS, ACE and DSCOVR. Using the minimum variance analysis (MVA) method on ACE's magnetic field, the normal directions are close to those derived from the cross product ($\hat{\mathbf{n}}_{\mathrm{TD}} = \pm \frac{\mathbf{B}_u \times \mathbf{B}_d}{|\mathbf{B}_u \times \mathbf{B}_d|}$). For the first discontinuity, we have $n_{1_{\mathrm{MVA}}} = \pm[0.90, -0.43, 0.02]$ and $n_{1_{\mathrm{TD}}} = \pm[0.80, -0.44, 0.40]$. The angle between the two normal directions is 22.6°, providing reasonable ground to assume that the first discontinuity is a TD. Measurement at DSCOVR shows that the normal direction of the first TD is $[0.64, -0.57, 0.51]$. Using the cross product method at THEMIS, the normal of the first TD (using background field on two sides of transient structures) is $n_{1_{\mathrm{THA}}} = \pm[0.65, -0.07, 0.76]$ or $n_{1_{\mathrm{THE}}} = \pm[0.68, 0.09, 0.73]$, which are roughly consistent with ACE and DSCOVR observations. The propagation time of the first TD from ACE to THEMIS is calculated to be 31.3 min, using $n_{1_{\mathrm{TD}}}$ and $V_{sw} = [-634.4, -15.4, -14.6]$ km/s, which roughly align with observed times (~40 min). The ~9 min discrepancy may arise from measurement uncertainty from ACE (which is currently not well calibrated), leading to a deviation from the correct direction in the calculation. From the DSCOVR data, the estimated duration is calculated to be 37.9 min, which agrees with the observation and is considered more reliable.

Approximately 5 min after the observations around the bow shock by THEMIS, MMS1 (located at [-7.9, 21.2, 6.3] R_E in GSE coordinates on the dusk side) in the magnetosheath detects the same magnetic field profile with an HFA core-like structure (Figure 5, marked in purple shadow). The density drops from ~7.0 cm^{-3} to 2.3 cm^{-3}, followed by an enhancement to 13.3 cm^{-3} (Figure 5C). The bulk velocity is slightly deflected, averaging to $V_{M'sh} = [-465.0, 183.7, 87.8]$ km/s (Figure 5D). Electron and ion temperatures are doubled in the low-density region compared to the ambient conditions (Figures 5E, F). The entire structure is pressure-balanced (Figure 5G). Some electrons are observed to be energized above 50 keV in the spectra around 08:36–08:38 UT (Figures 5I, J). The pitch angle of the energetic electrons is anti-parallel to the magnetic field within the structure and mainly parallel in the background (also see Supplementary Figure S3 in the supplementary material). Because the IMF is sunward, the localized anti-parallel asymmetry suggests that these energetic electrons locally originate from the bow shock side (Figure 5H), further confirming that the transient structure acts as an accelerator. Using the coplanarity method and the conservation of mass flux, the upstream boundary of the HFA moves in the direction of $\hat{\boldsymbol{n}}_s = [-0.93, 0.33, 0.15]$ at a speed $V_s = 153.0$km/s. The calculated time delay from the THEMIS location to MMS is ~6 min, based on the TD normal direction measured by DSCOVR, which is consistent with the observation.

THD on the downstream side of THA and THE (Figure 1O; around the same MLT sector) observes clear ULF waves (Figure 6C) in the magnetosphere [52], with a period comparable to the time

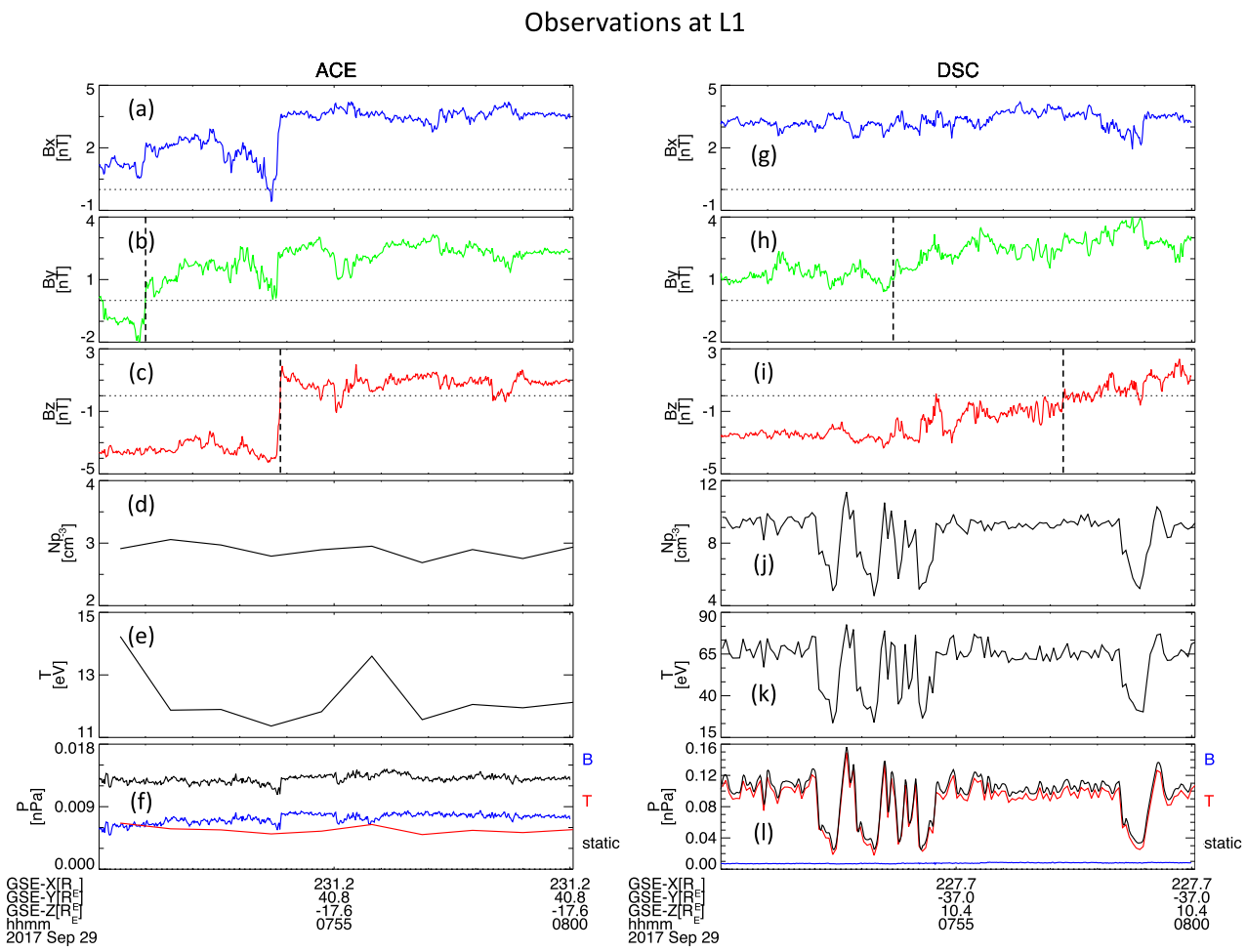

FIGURE 4
ACE and DSCOVR observations in the upstream solar wind. Panels **(A–C)** and **(G–I)** are magnetic field vectors in GSE coordinates. **(D, J)** are proton density, and **(E, K)** are proton temperatures. **(F, L)** show the magnetic pressures, thermal pressures and static pressures. Four dash lines mark two discontinuities across and after the transients.

scale of the MHD HFA. The velocity oscillations associated with the ULF waves (Figure 6E) modulate the energy of cold ions (Figure 6H), consistent with Wang et al. [17]. This modulation causes cold ion energy to periodically increase to levels detectable by ESA, thereby affecting the ion temperature (Figure 6F). These conjunction observations from THEMIS to MMS indicate that the transient structures are localized structures convecting with the discontinuities from the dawn side to the dusk side, continuously accelerating electrons and disturbing the local magnetosphere.

4 Discussion and summary

Using conjunction observations from three THEMIS spacecraft and one MMS spacecraft, we demonstrate that a kinetic FB and an MHD HFA can occur simultaneously, accelerating electrons up to 100 keV and locally disturbing the magnetosheath and magnetosphere while convecting from the dawn side to the dusk side with solar wind discontinuities. The coexistence of an FB and an HFA indicates the limitation of single spacecraft observations, which may not reveal the full scope of foreshock transients. For example, if only one spacecraft had been observing the small FB, the electron acceleration energy (~50 keV vs ~100 keV) and the scale (~1 min vs. ~3 min) of the disturbances in the bow shock, magnetosheath, and magnetosphere could have been significantly underestimated. The existence of MHD HFAs might also have been overlooked. In the future, more conjunction observations are essential to enhance our understanding of the formation and impacts of foreshock transients.

In the previous study, a 2.5-D global hybrid simulation reproduced both an FB and an HFA coexisting with a single discontinuity (see run 6 in [6]). We observe this situation for the first time. In the simulation, as a rotational discontinuity (RD) moves into the foreshock, a planar FB can form due to the interaction between the RD and the back-streaming ions. When the RD continues to convect and interacts with the bow shock, the FB dissipates while an HFA forms. The core of an FB can shift the displacements of the bow shock and magnetosheath outward due to its low dynamic pressure, potentially acting as a

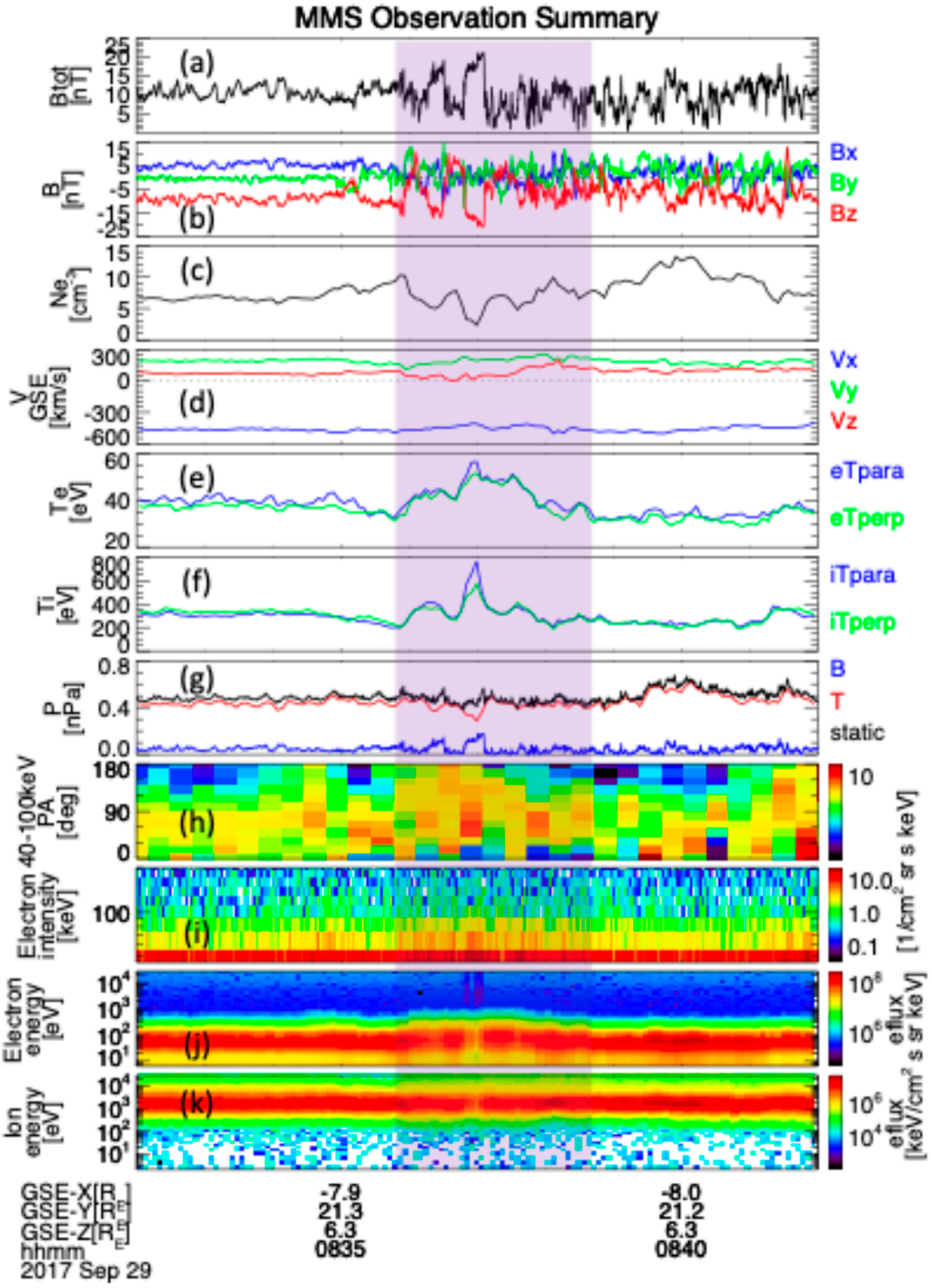

FIGURE 5
MMS observation in the magnetosheath. Panels are **(A)** magnetic field strength, **(B)** magnetic field vectors in GSE coordinates, **(C)** electron density, **(D)** ion bulk velocity, **(E)** electron temperatures, **(F)** ion temperatures, **(G)** magnetic pressure, thermal pressure and static pressure, **(H)** pitch angle of electrons between 40 and 100 keV, **(I)** electron intensity above 50 keV, **(J)** electron energy spectrum and **(K)** ion energy spectrum.

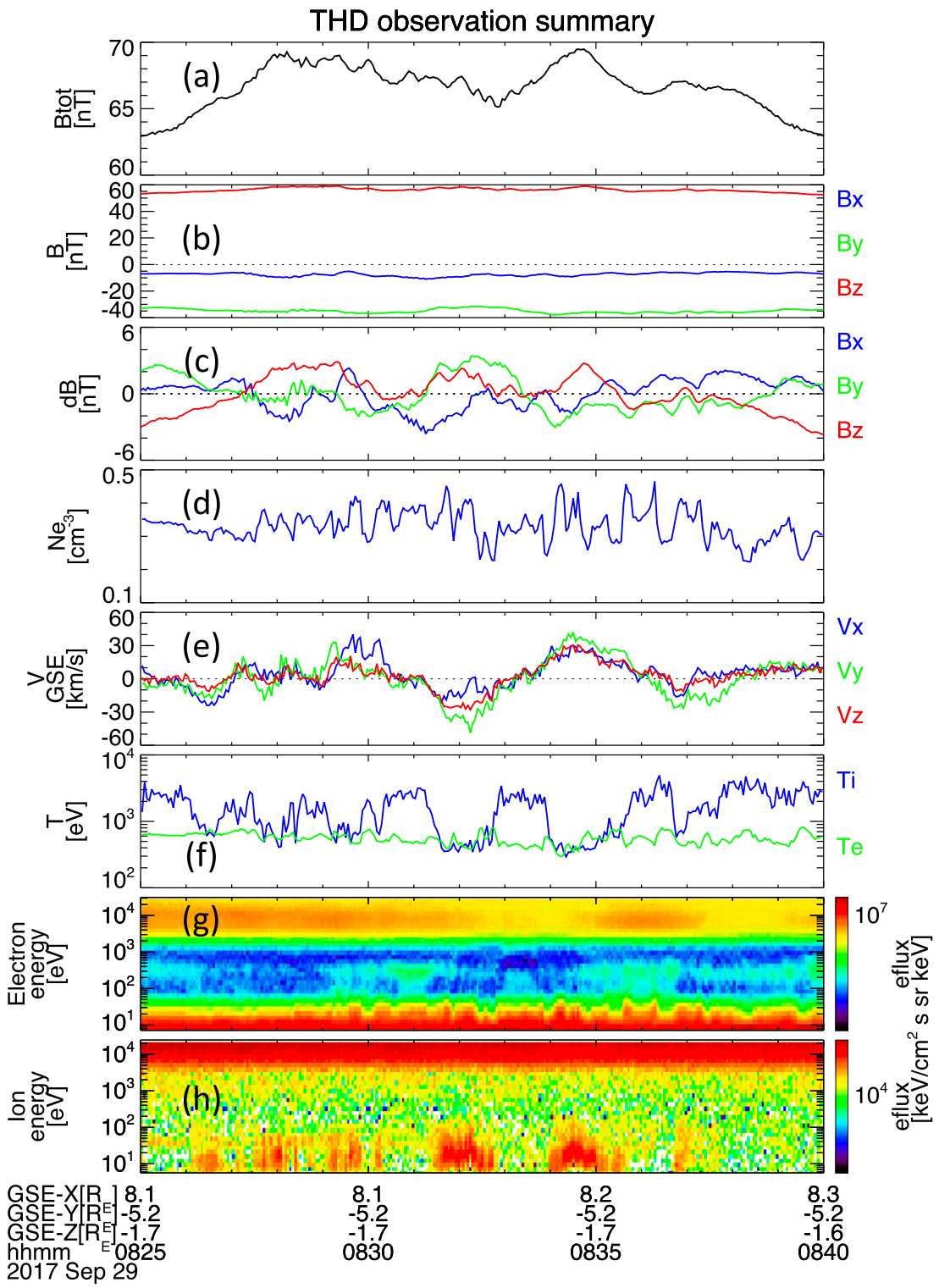

FIGURE 6
THD observation in the magnetosphere. Panels are **(A)** magnetic field strength, **(B)** magnetic field vectors in GSE coordinates, **(C)** magnetic field variations relative to the time average dB, **(D)** electron density, **(E)** ion bulk velocity, **(F)** ion and electron temperatures, **(G)** electron energy spectrum and **(H)** ion energy spectrum.

low-density flux tube that generates HFAs and explains the simultaneous observations. However, in our cases, the FB itself is unlikely large enough to be the direct driver, so there could be a combination of other processes. Previous observations and simulations by Otto and Zhang [28] indicate that a low-density flux tube can drive MHD HFAs, such as those observed by DSCOVR. This low-density flux tube does not have to be solar wind structures, but can also be some other foreshock transients, such as foreshock

density holes [29, 30, 33] and foreshock cavities [53]. Further analysis is still needed to uncover the mechanisms behind the coexistence of an FB and an HFA.

How electrons are accelerated to 100 keV around the bow shock remains an open question. Our results suggest a possibility of multi-step acceleration. Electrons may first be energized within a foreshock transient, e.g., through Fermi acceleration. As these electrons reach the bow shock along with the foreshock transient, the significant enhancement of field strength associated with the development of an MHD HFA may further energize them through betatron acceleration and other possible mechanisms. This scenario suggests that foreshock transients could energize electrons through an additional step when interacting with the bow shock, leading to higher acceleration capability than previously thought. Further observations and modeling efforts are needed to confirm this scenario.

Data availability statement

Publicly available datasets were analyzed in this study. This data can be found here: MMS data are available at MMS Science Data Center (https://lasp.colorado.edu/mms/sdc/public/). THEMIS data are available at http://themis.ssl.berkeley.edu/index.shtml. ACE and DSCOVR data are available at NASA's Coordinated Data Analysis Web (CDAWeb, https://cdaweb.gsfc.nasa.gov).

Author contributions

XL: Formal analysis, Investigation, Visualization, Writing-original draft, Writing–review and editing. TL: Conceptualization, Formal analysis, Funding acquisition, Investigation, Methodology, Validation, Writing–review and editing. XC: Writing–review and editing. AO: Conceptualization, Writing–review and editing. HZ: Conceptualization, Writing–review and editing.

Funding

The author(s) declare that financial support was received for the research, authorship, and/or publication of this article. This work was supported by NSF award AGS-2247760 to TL.

Acknowledgments

T.Z.L. acknowledges ISSI team led by Primoz Kajdic for helpful discussion. We thank the SPEDAS team and the NASA Coordinated Data Analysis Web (CDAWeb, http://cdaweb.gsfc.nasa.gov/). THEMIS dataset is available at https://themis.ssl.berkeley.edu/index.shtml. MMS dataset is available at https://lasp.colorado.edu/mms/sdc/public/.

Conflict of interest

The authors declare that the research was conducted in the absence of any commercial or financial relationships that could be construed as a potential conflict of interest.

Generative AI statement

The author(s) declare that no Generative AI was used in the creation of this manuscript.

Publisher's note

Supplementary material

The Supplementary Material for this article can be found online at: https://www.frontiersin.org/articles/10.3389/fphy.2024.1503092/full#supplementary-material

References

1. Schwartz SJ, Chaloner CP, Christiansen PJ, Coates AJ, Hall DS, Johnstone AD, et al. An active current sheet in the solar wind. *Nature* (1985) 318(6043):269–71. doi:10.1038/318269a0

2. Zhang H, Sibeck DG, Zong QG, Gary SP, McFadden JP, Larson D, et al. Time history of events and macroscale interactions during substorms observations of a series of hot flow anomaly events. *J Geophys Res Space Phys* (2010) 115(A12). doi:10.1029/2009ja015180

3. Liu Z, Turner DL, Angelopoulos V, Omidi N. THEMIS observations of tangential discontinuity-driven foreshock bubbles. *Geophys Res Lett* (2015) 42(19):7860–6. doi:10.1002/2015gl065842

4. Liu TZ, Turner DL, Angelopoulos V, Omidi N. Multipoint observations of the structure and evolution of foreshock bubbles and their relation to hot flow anomalies. *J Geophys Res Space Phys* (2016) 121(6):5489–509. doi:10.1002/2016ja022461

5. Omidi N, Eastwood JP, Sibeck DG. Foreshock bubbles and their global magnetospheric impacts. *J Geophys Res Space Phys* (2010) 115(A6). doi:10.1029/2009ja014828

6. Omidi N, Lee SH, Sibeck DG, Turner DL, Liu TZ, Angelopoulos V. Formation and topology of foreshock bubbles. *J Geophys Res Space Phys* (2020) 125(9):e2020JA028058. doi:10.1029/2020ja028058

7. Turner DL, Omidi N, Sibeck DG, Angelopoulos V. First observations of foreshock bubbles upstream of Earth's bow shock: characteristics and comparisons to HFAs. *J Geophys Res Space Phys* (2013) 118(4):1552–70. doi:10.1002/jgra.50198

8. Turner DL, Liu TZ, Wilson III LB, Cohen IJ, Gershman DG, Fennell JF, et al. Microscopic, multipoint characterization of foreshock bubbles with Magnetospheric Multiscale (MMS). *J Geophys Res Space Phys* (2020) 125(7):e2019JA027707. doi:10.1029/2019ja027707

9. Eastwood JP, Lucek EA, Mazelle C, Meziane K, Narita Y, Pickett J, et al. The foreshock. *Space Sci Rev* (2005) 118:41–94. doi:10.1007/s11214-005-3824-3

10. Schwartz SJ, Paschmann G, Sckopke N, Bauer TM, Dunlop M, Fazakerley AN, et al. Conditions for the formation of hot flow anomalies at Earth's bow shock. *J Geophys Res Space Phys* (2000) 105(A6):12639–50. doi:10.1029/1999ja000320

11. Facskó G, Nemeth Z, Erdős G, Kis A, Dandouras I. A global study of hot flow anomalies using Cluster multi-spacecraft measurements. *Ann geophysicae* (2009) 27(5):2057–76. doi:10.5194/angeo-27-2057-2009

12. Liu TZ, Wang CP, Wang B, Wang X, Zhang H, Lin Y, et al. ARTEMIS observations of foreshock transients in the midtail foreshock. *Geophys Res Lett* (2020) 47(21):e2020GL090393. doi:10.1029/2020gl090393

13. Archer MO, Turner DL, Eastwood JP, Schwartz SJ, Horbury TS. Global impacts of a foreshock bubble: magnetosheath, magnetopause and ground-based observations. *Planet Space Sci* (2015) 106:56–66. doi:10.1016/j.pss.2014.11.026

14. Thomas VA, Winske D, Thomsen MF, Onsager TG. Hybrid simulation of the formation of a hot flow anomaly. *J Geophys Res Space Phys* (1991) 96(A7):11625–32. doi:10.1029/91ja01092

15. Liu TZ, An X, Zhang H, Turner D. Magnetospheric multiscale observations of foreshock transients at their very early stage. *The Astrophysical J* (2020) 902(1):5. doi:10.3847/1538-4357/abb249

16. Omidi N, Sibeck DG. Formation of hot flow anomalies and solitary shocks. *J Geophys Res Space Phys* (2007) 112(A1). doi:10.1029/2006ja011663

17. Wang C-P, Wang X, Liu TZ, Lin Y. A foreshock bubble driven by an IMF tangential discontinuity: 3D global hybrid simulation. *Geophys Res Lett* (2021) 48:e2021GL093068. doi:10.1029/2021GL093068

18. Zhang H, Zong Q, Connor H, Delamere P, Facskó G, Han D, et al. Dayside transient phenomena and their impact on the magnetosphere and ionosphere. *Space Sci Rev* (2022) 218(5):40. doi:10.1007/s11214-021-00865-0

19. Vu A, Liu TZ, Zhang H, Delamere P. Hybrid simulations of a tangential discontinuity-driven foreshock bubble formation in comparison with a hot flow anomaly formation. *J Geophys Res Space Phys* (2022) 127(6):e2021JA029973. doi:10.1029/2021ja029973

20. Vu A, Liu TZ, Angelopoulos V, Zhang H. 2.5-D local hybrid simulations of hot flow anomalies under various magnetic field geometries. *J Geophys Res Space Phys* (2024) 129(5):e2023JA032301. doi:10.1029/2023ja032301

21. Liu TZ, Hietala H, Angelopoulos V, Turner DL. Observations of a new foreshock region upstream of a foreshock bubble's shock. *Geophys Res Lett* (2016) 43(10):4708–15. doi:10.1002/2016gl068984

22. Liu TZ, Lu S, Angelopoulos V, Hietala H, Wilson LB, III. Fermi acceleration of electrons inside foreshock transient cores. *J Geophys Res Space Phys* (2017) 122:9248–63. doi:10.1002/2017JA024480

23. Liu TZ, Lu S, Angelopoulos V, Lin Y, Wang XY. Ion acceleration inside foreshock transients. *J Geophys Res Space Phys* (2018) 123(1):163–78. doi:10.1002/2017ja024838

24. Liu TZ, Angelopoulos V, Lu S. Relativistic electrons generated at Earth's quasi-parallel bow shock. *Sci Adv* (2019) 5(7):eaaw1368. doi:10.1126/sciadv.aaw1368

25. Wang B, Liu T, Nishimura Y, Zhang H, Hartinger M, Shi X, et al. Global propagation of magnetospheric Pc5 ULF waves driven by foreshock transients. *J Geophys Res Space Phys* (2020) 125(12):e2020JA028411. doi:10.1029/2020ja028411

26. Wang B, Zhang H, Liu Z, Liu T, Li X, Angelopoulos V. Energy modulations of magnetospheric ions induced by foreshock transient-driven ultralow-frequency waves. *Geophys Res Lett* (2021) 48(10):e2021GL093913. doi:10.1029/2021gl093913

27. Wang B, Liu J, Han D, Wang Y, Feng X. Statistical study of hot flow anomaly induced ground magnetic ultra-low frequency oscillations. *J Geophys Res Space Phys* (2024) 129(8):e2024JA032667. doi:10.1029/2024ja032667

28. Otto A, Zhang H. Bow shock transients caused by solar wind dynamic pressure depletions. *J Atmos Solar-Terrestrial Phys* (2021) 218:105615. doi:10.1016/j.jastp.2021.105615

29. Lu X, Otto A, Zhang H, Liu T, Chen X. The bow shock and magnetosheath responses to density depletion structures. *J Geophys Res Space Phys* (2024) 129(5):e2024JA032566. doi:10.1029/2024ja032566

30. Lu X, Otto A, Zhang H, Liu T, Chen X. Observations and simulations of a double-core hot flow anomaly. *Geophys Res Lett* (2024) 51:e2024GL110363. doi:10.1029/2024GL110363

31. Sibeck DG, Phan TD, Lin R, Lepping RP, Szabo A. Wind observations of foreshock cavities: a case study. *J Geophys Res Space Phys* (2002) 107(A10). doi:10.1029/2001ja007539

32. Parks GK, Lee E, Mozer F, Wilber M, Lucek E, Dandouras I, et al. Larmor radius size density holes discovered in the solar wind upstream of Earth's bow shock. *Phys Plasmas* (2006) 13(5). doi:10.1063/1.2201056

33. Lu X, Zhang H, Liu T, Vu A, Pollock C, Wang B. Statistical study of foreshock density holes. *J Geophys Res Space Phys* (2022) 127(4):e2021JA029981. doi:10.1029/2021ja029981

34. McComas DJ, Bame SJ, Barker P, Feldman WC, Phillips JL, Riley P, et al. Solar wind electron proton alpha monitor (SWEPAM) for the Advanced Composition Explorer. In: *The advanced composition explorer mission* (1998).

35. Chiu MC, Von-Mehlem UI, Willey CE, Betenbaugh TM, Maynard JJ, Krein JA, et al. ACE spacecraft. *Space Sci Rev* (1998) 86:257–84. doi:10.1007/978-94-011-4762-0_13

36. Stone EC, Frandsen AM, Mewaldt RA, Christian ER, Margolies D, Ormes JF, et al. The advanced composition explorer. *Space Sci Rev* (1998) 86:1–22. doi:10.1007/978-94-011-4762-0_1

37. Valero FP, Herman J. DSCOVR, the first Deep space earth and solar observatory. *Cell Biol Instrumentation: UV Radiat Nitric Oxide Cell Death Plants* (2006) 371.

38. Burt J, Smith B. Deep space climate observatory: the DSCOVR mission. In: *2012 IEEE aerospace conference* (2012).

39. Smith CW, L'Heureux J, Ness NF, Acuna MH, Burlaga LF, Scheifele J. The ACE magnetic fields experiment. In: *The advanced composition explorer mission* (1998).

40. Angelopoulos V. *The THEMIS mission*. New York: Springer (2009).

41. McFadden JP, Carlson CW, Larson D, Ludlam M, Abiad R, Elliott B, et al. The THEMIS ESA plasma instrument and in-flight calibration. *Space Sci Rev* (2008) 141:277–302. doi:10.1007/s11214-008-9440-2

42. Auster HU, Glassmeier KH, Magnes W, Aydogar O, Baumjohann W, Constantinescu D, et al. The THEMIS fluxgate magnetometer. *Space Sci Rev* (2008) 141:235–64. doi:10.1007/s11214-008-9365-9

43. Angelopoulos V, Sibeck D, Carlson CW, McFadden JP, Larson D, Lin RP, et al. First results from the THEMIS mission. *Space Sci Rev* (2008) 141:453–76. doi:10.1007/s11214-008-9378-4

44. Burch JL, Moore TE, Torbert RB, Giles BH. Magnetospheric multiscale overview and science objectives. *Space Sci Rev* (2016) 199:5–21. doi:10.1007/s11214-015-0164-9

45. Pollock C, Moore T, Jacques A, Burch J, Gliese U, Saito Y, et al. Fast plasma investigation for magnetospheric multiscale. *Space Sci Rev* (2016) 199:331–406. doi:10.1007/s11214-016-0245-4

46. Torbert RB, Russell CT, Magnes W, Ergun RE, Lindqvist PA, LeContel O, et al. The FIELDS instrument suite on MMS: scientific objectives, measurements, and data products. *Space Sci Rev* (2016) 199:105–35. doi:10.1007/s11214-014-0109-8

47. Mauk BH, Blake JB, Baker DN, Clemmons JH, Reeves GD, Spence HE, et al. The energetic particle detector (EPD) investigation and the energetic ion spectrometer (EIS) for the magnetospheric multiscale (MMS) mission. *Space Sci Rev* (2016) 199:471–514. doi:10.1007/s11214-014-0055-5

48. Wu DJ, Chao JK, Lepping RP. Interaction between an interplanetary magnetic cloud and the Earth's magnetosphere: motions of the bow shock. *J Geophys Res Space Phys* (2000) 105(A6):12627–38. doi:10.1029/1999ja000265

49. Shue JH, Song P, Russell CT, Steinberg JT, Chao JK, Zastenker G, et al. Magnetopause location under extreme solar wind conditions. *J Geophys Res Space Phys* (1998) 103(A8):17691–700. doi:10.1029/98ja01103

50. Bittencourt JA. *Fundamentals of plasma physics*. Springer Science and Business Media (2013).

51. Liu TZ, Angelopoulos V, Vu A, Zhang H, Otto A, Zhang K. THEMIS observations of magnetosheath-origin foreshock ions. *J Geophys Res Space Phys* (2024) 129(2):e2023JA031969. doi:10.1029/2023ja031969

52. Hartinger MD, Turner DL, Plaschke F, Angelopoulos V, Singer H. The role of transient ion foreshock phenomena in driving Pc5 ULF wave activity. *J Geophys Res Space Phys* (2013) 118:299–312. doi:10.1029/2012JA018349

53. Sibeck DG, Lee SH, Omidi N, Angelopoulos V. Foreshock cavities: direct transmission through the bow shock. *J Geophys Res Space Phys* (2021) 126(5):e2021JA029201. doi:10.1029/2021ja029201